Lawrence Berkeley National Laboratory

LBL Publications

Title
Atomic layer deposition of 2D and 3D standards for synchrotron-based quantitative composition and structure analysis methods

Permalink
https://escholarship.org/uc/item/2c4971xf

Journal
Journal of Vacuum Science & Technology A Vacuum Surfaces and Films, 36(2)

ISSN
0734-2101

Authors
Becker, Nicholas G
Butterworth, Anna L
Salome, Murielle
et al.

Publication Date
2018-03-01

DOI
10.1116/1.5025240

Peer reviewed

eScholarship.org   **Powered by the California Digital Library**
University of California

Atomic layer deposition of 2D and 3D standards for synchrotron-based quantitative composition and structure analysis methods

Nicholas G. Becker, Anna L. Butterworth, Murielle Salome, Stephen R. Sutton, Vincent De Andrade, Andrey Sokolov, Andrew J. Westphal, and Thomas Proslier

---

ARTICLES YOU MAY BE INTERESTED IN

Review Article: Stress in thin films and coatings: Current status, challenges, and prospects
Journal of Vacuum Science & Technology A **36**, 020801 (2018); https://doi.org/10.1116/1.5011790

Initial reactions of ultrathin HfO_2 films by in situ atomic layer deposition: An in situ synchrotron photoemission spectroscopy study
Journal of Vacuum Science & Technology A: Vacuum, Surfaces, and Films **36**, 02D402 (2018); https://doi.org/10.1116/1.5015946

Atomic layer deposition of molybdenum disulfide films using MoF_6 and H_2S
Journal of Vacuum Science & Technology A **36**, 01A125 (2018); https://doi.org/10.1116/1.5003423

In-system photoelectron spectroscopy study of tin oxide layers produced from tetrakis(dimethylamino)tin by plasma enhanced atomic layer deposition
Journal of Vacuum Science & Technology A: Vacuum, Surfaces, and Films **36**, 02D401 (2018); https://doi.org/10.1116/1.5015967

Effect of ion energies on the film properties of titanium dioxides synthesized via plasma enhanced atomic layer deposition
Journal of Vacuum Science & Technology A **36**, 021515 (2018); https://doi.org/10.1116/1.5001552

Atomic layer deposition of AlN from $AlCl_3$ using NH_3 and Ar/NH_3 plasma
Journal of Vacuum Science & Technology A **36**, 021508 (2018); https://doi.org/10.1116/1.5003381

Atomic layer deposition of 2D and 3D standards for synchrotron-based quantitative composition and structure analysis methods

Nicholas G. Becker
Physics Department, Illinois Institute of Technology, Chicago, Illinois 60616

Anna L. Butterworth
Lawrence Berkley National Laboratory, Berkley, California 94720

Murielle Salome
European Synchrotron Radiation Facility, Grenoble 38000, France

Stephen R. Sutton
GSECARS, University of Chicago, Argonne, Illinois 60439

Vincent De Andrade
X-Ray Science Department, Advanced Photon Source, Argonne National Laboratory, Lemont, Illinois 60439

Andrey Sokolov
Material Science Division, Argonne National Laboratory, Argonne, Illinois 60439

Andrew J. Westphal
Lawrence Berkley National Laboratory, Berkley, California 94720

Thomas Proslier[a)]
Commissariat de l'énergie atomique, Centre de Saclay, Gif-sur-Yvette 91191, France

Atomic layer deposition (ALD) is a scalable deposition technique known for producing uniform, conformal films of a wide range of compounds on nearly any substrate material. These traits make it an ideal deposition method for producing films to replace the National Institute of Standards and Technology (NIST) standards and create Standard Reference Materials (SRMs) on a wide range of relevant two-dimensional and three-dimensional substrates. The use of SRM from NIST for quantitative analysis of chemical composition using synchrotron based x-ray fluorescence (SR-XRF) and scanning transmission x-ray microscopy (STXM) is common. Such standards, however, can suffer from inhomogeneity in chemical composition and thickness and often require further calculations, based on sample mounting and detector geometry, to obtain quantitative results. These inhomogeneities negatively impact the reproducibility of the measurements and the quantitative measure itself. Utilizing Rutherford backscattering, x-ray reflectivity, quartz crystal microbalance, STXM, and SR-XRF, the authors show that ALD is capable of producing high quality standards that are homogenous over scales ranging from nanometers to 100s of micrometers. *Published by the AVS.*
https://doi.org/10.1116/1.5025240

I. INTRODUCTION

Synchrotron based x-ray fluorescence (SR-XRF) and scanning transmission x-ray microscopy (STXM) are two powerful techniques that have chemical speciation resolution capabilities from hundreds of microns to tens of nanometers.[1–6] These techniques allow for the speciation and quantification of major and trace elements, in a vacuum and ambient environments, with detection limits on the order of parts per million. STXM can be viewed as a combination of soft x-ray absorption spectroscopy and submicron microscopy[3] with chemical spatial resolution down to tens of nanometers.[7] This technique is used in fields ranging from characterization of basaltic glass[1] to *in situ* investigation of organic field effect transistors.[4] SR-XRF can operate at higher energies, with spatial resolution on the order of hundreds of nanometers. Ergo, SR-XRF is utilized in a variety of fields, including the visualization of lost paintings,[6] the quantification of trace elements in individual protist

cells,[8] the study of metal homeostasis in plants,[9] and the distribution patterns of trace elements, such as Arsenic, in rice.[10]

Driving our motivation for new standards was the challenge of intercalibration of quantitative STXM and SR-XRF analyses of the same picogram sample.[11,12] A consortium, "Stardust Interstellar Preliminary Examination" or ISPE, characterized probable interstellar particles captured by the NASA Stardust Mission.[13] ISPE analyzed major rock-forming elements Mg, Al (K-edges), and Fe (L-edge) by STXM and less abundant, heavier ($Z > Ca$) elements by SR-XRF. The picogram-sized interstellar dust particle samples could not be analyzed by any other techniques due to the required sensitivity and sample preservation. Only one element, Fe, present in these samples was measurable by both synchrotron techniques (>3 fg/μm^2 Fe by STXM and SR-XRF). By comparing independent, calibrated Fe measurements on the same sample, the elemental abundance datasets from the two techniques could be combined for a more complete elemental characterization of the samples. However, existing SR-XRF Fe standards were either too thick for

STXM analyses, which require thinner than $1.5 \, pg/\mu m^2$ Fe, or not sufficiently homogenous for comparing nanometer- to micrometer-spot sized analyses across techniques.

These techniques however suffer from the inability to quantitatively measure constituents without the use of standards of some known areal density, usually expressed in $\mu g/cm^2$. The majority of research done using these techniques utilizes either National Institute of Standards and Technology (NIST) produced thin film two-dimensional (2D) standards or solution based standards that are then diluted and measured, either in solution or after drying on an appropriate substrate. In either case, the assumption is that the standard is homogenous on large and small scales. In addition, the rapid development of nanoscale three-dimensional (3D) imaging transmission X-Ray microscopy (TXM) techniques and powerful reconstruction algorithms for nanomaterial sciences in the field of energy storage, microelectronics, light harvesting materials calls for the development of new 3D standards of known shape and composition.

Regardless of the standard, algorithms must be used to correct for the difference in absorption between the reference and the sample using a fundamental parameter approach. Further complications arise when the standard reference material (SRM) does not exist for a specific element of interest. In these cases, the use of an SRM with elements that have atomic numbers above and below the element of interest, along with software packages to extrapolate the sensitivity for the element of interest, allows for quantitative determinations.[9]

Atomic layer deposition (ALD) is a self-limiting, vapor deposition technique that pulses consecutive doses of chemical reagents to deposit thin films in a layer-by-layer fashion. It is characterized by large area uniformity, conformality over arbitrarily complex-shaped samples, and atomic scale thickness control.[14–16] The library of materials that can be deposited via ALD is extensive and encompasses the majority of the nonradioactive portion of the periodic table.[17] These unique capabilities have been used in a large variety of applications for which atomic scale thickness and composition control at industry production levels (over hundreds of square meters) is crucial.[18–25] Part of the beauty of the ALD approach is the flexibility in selecting substrates ideal for the synchrotron techniques as opposed to being constrained by the standards themselves. Here, we report on the measurement of thin ALD film uniformity deposited on thin, flat, transmission electron microscope (TEM) membranes and 3D cubes made by 3D printing with the goal of replacing the conventional 2D SR-XRF and STXM standards as well as creating new 3D standards in anticipation of future advances in 3D imaging synchrotron techniques.

II. EXPERIMENT

ALD films were grown in a commercial UltraTech (formerly Cambridge NanoTech) Savannah 100 or a custom-built flow reactor described elsewhere.[19] The UltraTech system has been modified to accept bubbler type precursor cylinders to aid in the deposition of compounds using low vapor pressure precursors. Chemicals were obtained from Strem Chemicals and Sigma Aldrich and used as received. Unless otherwise noted, precursors were held in stainless steel cylinders. All compounds were prepared using previously disclosed ALD chemistries, listed in Table I.

A. 2D Standards

The 50 nm thick Si_3N_4 TEM windows were obtained from Norcada@ (part# NH050A3 and NT050C) [Figs. 1(a) and 1(b)] and used as received. These perforated or holey (sic) TEM windows allow for the concurrent measurement of the incident beam intensity, I_0, and normalization in STXM data acquisition, necessary for high precision measurements. The TEM windows were held in a specially designed stainless steel holder to keep four TEM windows in place during the cycling from the ALD deposition pressure of 1 Torr to atmosphere and are shown in Figs. 1(c) and 1(d). The pumping and venting of the ALD chamber have to be done gradually and slowly to avoid breakage of the thin TEM windows. Films were simultaneously deposited on 400 μm thick Si (001) and sometimes Si_3N_4 coupons which were cleaned via sonication in acetone and isopropanol and then rinsed with deionized water. Prior to depositing targeted standard films, the substrates were

TABLE I. Precursor chemistries, dose time, purge time, and deposition temperature for all compounds measured. These parameters are for 2D standards unless otherwise noted.

Compound	Metal precursor [dose(s)/purge(s)]	Oxygen/nitrogen source [dose(s)/purge(s)]	Deposition temperature (°C)	References
Fe_2O_3[a]	$FeCl_3$[b] (2/60)	H_2O (0.1/60)	250	26
Fe_2O_3[c]	$FeCl_3$[b] (3/20)	H_2O (0.1/60)	300	26
Y_2O_3[c]	$Y(Cp)_3$[b] (3/20)	H_2O (2/20)	250	25
TiO_2[c]	$TiCl_4$ (2/20)	H_2O (2/20)	250	27
Al_2O_3[a]	TMA (0.1/20)	H_2O (0.1/20)	200	23
Al_2O_3[c,d]	TMA (1/10)	H_2O (1/10)	165	23
ZnO[a]	DEZ (0.2/60)	H_2O (1/10)	140	23
ZnO[a]	DEZ (1/10)	H_2O (1/10)	165	23
MgO[c]	$Mg(Cp)_2$[b] (1.5/25)	H_2O (1/20)	250	28
Er_2O_3[c]	$Er(MeCp)_3$[b] (2/25)	H_2O (1/15)	250	29
MoN[c]	$MoCl_5$[b] 1.5/15	NH_3 (1/15)	450	30

[a]UltraTech reactor.
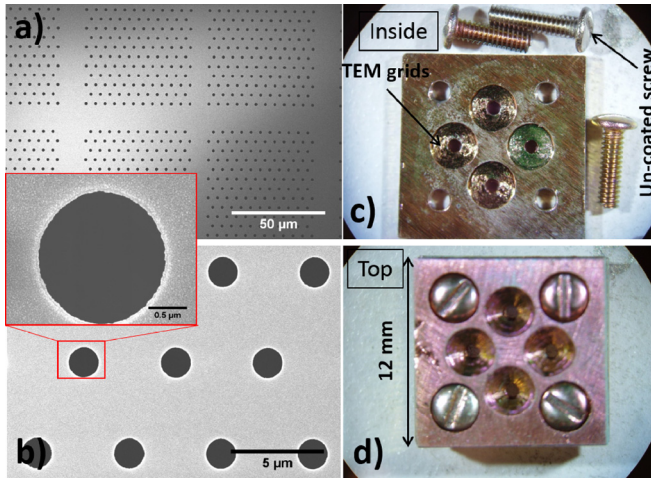[b]Held in the bubbler style cylinder.
[c]Custom built reactor.
[d]3D standard.

FIG. 1. (Color online) (a) and (b) SEM images of a half holey TEM Si_3N_4 window coated with 300 cycles of ZnO. (c) and (d) The TEM window holder used for ALD depositions. Note the uniformity of the window holder color due to the previous ALD depositions, indicative of a homogeneous coating even on the screws' threads (an uncoated screw is shown for comparison).

coated with a thin (20 cycles) Al_2O_3 layer to alleviate thickness uncertainty that could arise from poor nucleation on inert Si_3N_4.

STXM measurements were done at the Advanced Light Source (ALS), beamline 11.0.2, where the L-edges of iron and zinc and the K-edges of aluminum were investigated. SR-XRF measurements of yttrium, iron, and zinc were carried out at both the ALS, beamlines 5.3.2.1 and 10.3.2, and the Advanced Photon Source (APS), beamline 13ID, where titanium SR-XRF was also collected.

The areal (or columnar) density is determined by measuring the optical density across an edge jump. In all cases, the measured areal densities (μg/cm^2) are expected to be double that deposited on a silicon witness piece due to the conformal nature of ALD where both sides of the TEM windows are coated during a deposition. For a given sample, the optical density, OD, at a given position is

$$OD = \mu \times \rho \times t = -\ln\left(\frac{I}{I_0}\right), \quad (1)$$

where μ is the absorption cross-section, ρ is the density in g/cm^3, t is the thickness, I is the measured transmitted intensity, and I_0 is the incident intensity. The absorption cross-section changes with incident energy, and by fitting the change for any given edge jump, areal density can be obtained.

ALS measurements were analyzed using the AXIS2000 software package. The mass absorption coefficient, μ, is obtained from Ref. 31 and is also available within the AXIS2000 software. Areal density is computed using a two-component fit of an OD spectrum with the computed mass absorption coefficient spectra, μ, for: (1) the element of interest and (2) the major composition of the sample contributing to the pre-edge. This fitting procedure removes the pre-edge portion of the spectrum and allows for the fitting of the postedge, with extrapolation back to the edge

jump, such that the magnitude of the optical density can be calculated.

The APS measurements were performed in a similar manner, but instead of using calculated absorption coefficients, a thin film reference standard from NIST (NIST SRM-1833) was utilized, making the measurement as free of assumptions as possible. In both cases, the areal density, $\rho \times t$, was computed.

The NIST standards are tested using multiple analytical techniques (atomic absorption spectrometry, inductively coupled plasma emission spectrometry, neutron activation analysis, direct current plasma emission spectrometry, and isotope dilution thermal ionization mass spectrometry), and a percent uncertainty is provided with the certificate of analysis.

The error associated with the AXIS2000 fitting procedure arises from both the fit itself, with a quoted 1 σ error, and the tabulated values of μ, $\pm10\%$. The precision of the measurements depends on the signal to noise ratio of the spectrum and varies widely (5%–100%) depending on the thickness, the particular edge, and the abundance of the element. To insure the greatest measurement precision, the ALD films were deposited with an "optimal" OD value between 0.1 and 2.0, for which the count detection calibrations are linear.

The μ-XRF measurements of Mg (K-edge), Er (M-edge), and Mo (L-edge) were done at the European Synchrotron Radiation Facility (ESRF) beamline 21 at an energy of 2.7 keV, and the beam was focused with Kirkpatrick-Baez mirrors down to 0.6×0.84 μm. The detector is a Bruker Silicon drift diode collimated to 80 mm^2. A 100 s static spectrum and a 2D map with 1 μm steps over 50×50 μm^2 with 300 ms integration time per point were acquired for each sample. The spectra and maps were fitted with PyMCA (Ref. 32) to deconvolve the elemental maps. The mass fraction of the respective elements was calculated using a NIST standard and considering a 50 nm Si_3N_4 matrix then converted to μg/cm^2 by multiplying the mass fractions by the matrix density (3.25 g/cm^3) for Si_3N_4 and thickness (50 nm). The obtained results were then normalized to the I_0 map and multiplied by the iodet value corresponding to the photon flux used in the PyMCA configuration file. Several methods were used to measure independently the element areal density on flat Si or Si_3N_4 coupons grown at the same time as the TEM windows.

Rutherford backscattering (RBS) measurements were performed on silicon witness pieces by Evans Analytical Group using a 2.275 MeV He^{++} ion beam, normal to the sample surface and a backscatter detector oriented at 160° or at 110°. Values for the areal density of the metal ions, A_d, were then calculated from the atomic areal density of the oxide, ρ_{RBS}, the atomic mass, m_a, Avogadro's number, N_A, and the reported percentage of the ion of interest, x, using the following equation:

$$A_d = x \times \frac{\rho_{RBS} \times m_a}{N_A}. \quad (2)$$

RBS measurement errors given by Evans Analytical are 1% for Al, Zn, Fe, Y, Ti, and Mg and 0.5% for Mo and Er.

X-ray reflectivity (XRR) is another method used to obtain the elemental areal density with the following equation:

$$A_d = \frac{\rho_{XRR} \times t \times m_b}{m_b + \eta \times m_a}, \tag{3}$$

where ρ_{XRR} is the film density in g/cm^3, t is the film thickness, and m_a and m_b are the atomic mass of elements a and b. η is the element a stoichiometry normalized to b; for instance, for $Y_2O_3 = YO\eta$ with $\eta = 1.5$. XRR measurements were performed on a Philips X'Pert Pro MRD diffractometer using Cu Kα radiation $\lambda = 1.5418$ Å and operated at 30 kV/30 mA. The incident x-ray beam was conditioned by a 60 mm graded parabolic W/Si mirror with a 0.8° acceptance angle and a 1/32° divergence slit. The reflected beam was collected with a PW3011/20 sealed proportional point detector positioned behind a 0.27° parallel plate collimator and a pyrolytic graphite monochromator. The fit errors are calculated using the Panalytical reflectivity program X'Pert Reflectivity.

Finally, *in situ* quartz crystal microbalance (QCM) was used to monitor the ALD film growth. QCM measures in real time the deposited alloy areal density A_{QCM}, and the element specific areal density can be obtained by

$$A_d = \frac{A_{dQCM} \times m_b}{m_b + \eta \times m_a}. \tag{4}$$

Due to the design of the custom built ALD flow reactor, the QCM measurements were not done simultaneously with the thin film standard growth but under the same conditions (temperature, pressure, dose, and purge times). The error associated with the QCM measurement is the standard deviation from the average of the mass gain per cycle calculated over a large number of cycles.

B. 3D standards

The 3D standards were made using the 3D printer model *Photonic Professional GT* from Nanoscribe@ that enables 3D micro- and nanofabrication via two-photon polymerization. The shape of a cube with the corresponding edges presented in Fig. 2(b) was chosen as a reference structure that provides different line directions with respect to the x-ray beam [represented by an arrow in Fig. 2(b)] in order to test the reconstruction algorithm. This structure, 5.7 μm side size, was 3D printed at the apex of a Tungsten tip with a radius of curvature of 1 μm [Fig. 2(a)]. The tip was laid down horizontally on a glass substrate, maintained immobile with a tape, and immersed in the photoresist IP-L 780. The W tip was aligned carefully with respect to the laser beam (780 nm, the same direction as the x-ray arrow) focal point at low power prior to starting the writing process with the parameters: 25% of the maximal laser power and a power scaling of 0.9. The tip was moved by a piezo stage with respect to a stationary focused laser beam in an optimal writing speed range between 20 and 30 μm/s.

The shape of the laser focal point, so-called vertex, is an ellipsoid with a nominal minimal size of $\sim$1 μm along the laser beam direction and $\sim$0.3 μm in the perpendicular plane. The vertex shape is responsible for the cube edge asymmetry and flattened aspect. As can be seen in Fig. 2(b), we choose
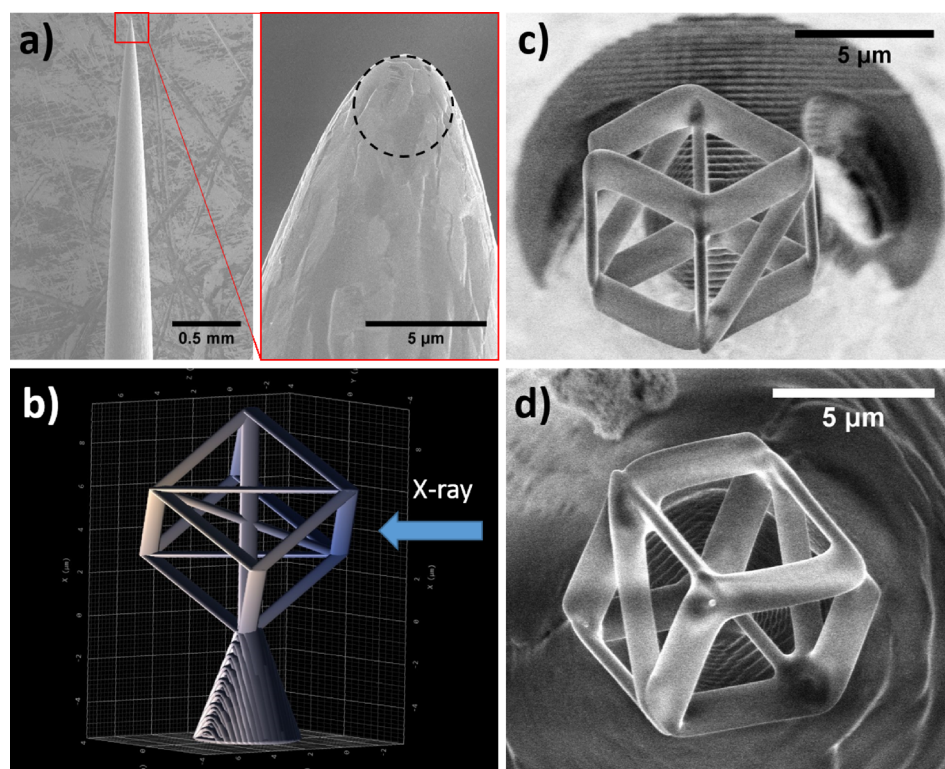

FIG. 2. (Color online) (a) SEM image of a W tip with a curvature radius of 2 μm. (b) representation of the 3D cube structure from the Nanoscribe@ laser writing software. (c) and (d) SEM images of two cubes viewed from the top after the laser writer and development process.

TABLE II. Multilayer ALD parameters deposited on the 3D cube.

Compound	ALD cycles	Targeted t (nm)	Measured t (nm)	Measured GR (Å/cycle)
Al_2O_3	50	5	6.06 ± 0.014	1.21 ± 0.003
ZnO	28	5	4.13 ± 0.014	1.47 ± 0.005
Al_2O_3	100	10	12.07 ± 0.028	1.2 ± 0.003
ZnO	55	10	8.54 ± 0.033	1.55 ± 0.006
Al_2O_3	160	16	19.2 ± 0.12	1.2 ± 0.007
ZnO	111	20	17.2 ± 0.15	1.55 ± 0.013
Al_2O_3	400	40	38.5 ± 10.3	0.96 ± 0.26
ZnO	222	40	34.5	1.55
Al_2O_3	800	80	78.6	0.98
ZnO	444	80	74.6	1.68

to start the writing process before the tip apex in order to anchor the cube on the tip and provide better stability during future handling. The structures were then developed by dipping the tips into PGMEA for 30 min, then cleaned with isopropanol, and dried in air. After about five optimization attempts, three cubes were successfully printed among which two are presented in Figs. 2(c) and 2(d). The measured cube side and edge dimensions are 5.6 μm and 0.5 × 1.5 μm, respectively, in close agreement with the nominal design specifications.

The tips were then inserted into the custom-built ALD chamber, and a multilayer composed of Al_2O_3 and ZnO was deposited at 165 °C with the targeted thicknesses, t, and deposition parameters summarized in Table II. The actual layer thicknesses and the corresponding ALD growth rates (GR) were measured by x-ray reflectivity on witness Si coupons. The fitting program was unable to calculate the error for the three thicker layers listed in Table II.

The TXM measurements were made at the Advanced Photon Source at beamline 32-ID-C.[33] The dataset consists of 1501 projections with 500 ms exposure acquired at 8 keV in the absorption mode. The x-ray objective lens of the microscope was a 180 μm large Fresnel zone plate with an outermost zone width of 60 nm and a thickness of 1.4 μm for an efficiency of ~18%. The 2D optical resolution is around 60 nm. Reconstruction was performed using the toolkit Tomopy[34,35] calling a ring artifact removal algorithm[36] and the sirt-fbp reconstruction algorithm.[37–39] The reconstructed volume has a voxel size of 28 nm.

III. RESULTS AND DISCUSSION

A. 2D Standards

Two types of standards were constructed, single compound films and multilayer films. When constructing multilayer standards, some consideration as to order must be given to eliminate possible detrimental surface reactions.[23] In Table III, compounds denoted with [b], [d], and [e] are portions of the same multilayer films. ALD enables the synthesis of multilayer structures with various growth sequences; either the films are grown sequentially as it was done in [b] as follows: Substrate\$Al_2O_3$-20 cycles\ZnO-150 cycles\$TiO_2$-250 cycles\$Y_2O_3$-500 cycles\$Fe_2O_3$-300 cycles, and in [d]: Substrate\

Al_2O_3-600 cycles\ZnO-150 cycles\$Fe_2O_3$-300 cycles or the various alloys can be diluted into a matrix such as in the multilayer [e]: Substrate\$Al_2O_3$-20 cycles\60 × {20 cycles MgO + 1 cycles Er_2O_3}. Although the sequence itself does not matter for a targeted element areal density (as long as the growth processes are well controlled), the diluted approach highlights the minimal deposition possible by ALD, i.e., one ALD cycle, which varies typically between 10 and 100 ng/cm^2/cycles depending on the material synthesized. This quantum of areal density deposited, listed for each cation element in Table III, sets the sensitivity limit for very low concentration standards made with one ALD cycle into an arbitrary matrix. One needs to be careful however as, in some cases,[14] the nucleation of a small number of ALD cycles might feature a different growth behavior. As a result, the measured areal density would deviate from the intended one.

The results from the STXM/SR-XRF measurements on TEM windows and those measured by RBS, XRR, and QCM on silicon witness pieces are given in Table III and summarized in Fig. 3. The fitting and measurement uncertainty of the RBS, XRR, and QCM techniques are taken into account in the errors listed. These three techniques give very consistent results with an average uncertainty of 1.1 ± 0.6%, which is about 1 order of magnitude smaller than the STXM/XRF measurements and analysis errors using the NIST standards: 12 ± 7.8%. All measured areal density values on silicon witness pieces are in good agreement with the STXM/XRF ones on TEM windows. Some systematic difference however exists which could be attributed to several factors: variation in the NIST calibration standards and fitting procedures used in STXM/XRF analysis or nonconformal coating by the deposition method. The latter factor has been seen previously[14] when the deposition temperature is outside the ALD regime and is discussed later in more detail. Within the former factor, it is important to mention that the possibility of small scale variation outside of the percent uncertainty listed cannot be ignored. This is particularly important in STXM or μSR-XRF where the measurement can be very localized. STXM and SR-XRF measurements were carried out on a TEM membrane and a Silicon witness piece, respectively, both coated simultaneously with Fe_2O_3. The STXM measurement yields an areal density value of 14.2 μg/cm^2, exactly double the one obtained with the SR-XRF measurement, 7.1 μg/cm^2. This is to be expected as ALD coats conformally both sides of the thin TEM windows and STXM probes the full structure thickness: (thin films coating)\TEM window (50 nm)\(thin films coating), whereas SR-XRF probes only one side of the ALD coated 400 μm thick witness silicon coupon.

This result comforts the fact that ALD coating inhomogeneity cannot be the source of discrepancy mentioned earlier and further emphasizes the need for new, reliable standards in STXM/XRF quantitative analysis.

All ALD depositions were carried out at temperatures within this self-limiting window, which should eliminate the possibility of parasitic chemical vapor deposition (CVD) and the inhomogeneous coating associated during the ALD process. The substrate heating due to the exothermic nature of

TABLE III. Areal density values, A_d in $\mu g/cm^2$, measured via STXM/XRF on TEM windows and compared with those measured on silicon witness coupons with RBS, XRR, and QCM and extracted using Eqs. (2)–(4). The minimal areal density deposited per ALD cycle for each cation, so-called Quantum ALD A_d, is in ng/cm^2 cycles and corresponds to the average of the RBS, XRR, and QCM measurements divided by the number of ALD cycles.

Film	Cation	A_d STXM/XRF	A_d RBS	A_d XRR	A_d QCM	Quantum ALD A_d
Fe_2O_3	Fe	14.2 ± 1.42^a	15.8 ± 0.16	15.3 ± 0.16	15.8 ± 0.4	26.4 ± 0.8
$Fe_2O_3{}^b$	Fe	10.8 ± 0.35^c	10.7 ± 0.1	10.73 ± 0.06	10.4 ± 0.18	26.5 ± 0.3
$Y_2O_3{}^b$	Y	39.09 ± 3.91^c	34.4 ± 0.35	35.5 ± 1.1	36.8 ± 0.8	35.6 ± 1.4
$TiO_2{}^b$	Ti	8.6 ± 1.21^c	8.07 ± 0.1	8.18 ± 0.1	8.1 ± 0.15	16.4 ± 0.3
ZnO^b	Zn	25.05 ± 2.08^b	24.72 ± 0.24	24.8 ± 0.07	24.6 ± 0.08	83.2 ± 0.8
ZnO	Zn	55.3 ± 5.53^a	52.2 ± 0.5	54.5 ± 0.11	53.1 ± 0.1	87.8 ± 0.5
$Al_2O_3{}^d$	Al	16.7 ± 1.7^a	18.9 ± 0.2	20.03 ± 0.04	19.4 ± 0.1	21 ± 0.2
$Fe_2O_3{}^d$	Fe	6 ± 1^a	9.66 ± 0.1	9.65 ± 0.06	10.4 ± 0.18	24.5 ± 0.3
ZnO^d	Zn	16 ± 6^a	24.1 ± 0.24	23.8 ± 0.07	24.6 ± 0.08	85.2 ± 0.8
MgO	Mg	28.3 ± 3^e	19.8 ± 0.2	19.5 ± 0.4	20.1 ± 0.15	19.8 ± 0.3
MgO^f	Mg	59.4 ± 6^e	47.5 ± 0.5	47.1 ± 0.2	48.0 ± 0.28	19.8 ± 0.16
$Er_2O_3{}^f$	Er	8 ± 0.8^e	11 ± 0.06	10.9 ± 0.1	11.1 ± 0.12	91.6 ± 0.7
$Er_2O_3{}^e$	Er	61.9 ± 6^e	90.5 ± 0.5	89.8 ± 0.6	92.3 ± 2	90.6 ± 0.14
MoN^e	Mo	112.5 ± 10^e	95.6 ± 0.5	96 ± 1.6	NA	23.3 ± 1.25

[a]Value measured at ALS (STXM).
[b]Part of the same multilayer.
[c]Value measured at APS (SR-XRF).
[d]Part of the same multilayer.
[e]Value measured at ESRF (SR-μXRF).
[f]Part of the same multilayer.

ALD reactions however may play a role. A simple formula for the change in temperature as a function of substrate, thickness t, density ρ, change in enthalpy ΔH, number of reaction sites σ, and specific heat of the substrate c is given in the following equation:

$$\Delta T = \frac{2 \times \sigma \times \Delta H}{c \times N_A \times \rho \times t}, \qquad (5)$$

where N_A is Avogadro's number and the factor of two comes from the coating of both sides of the TEM window. This formula assumes that all the chemical energy is deposited as heat
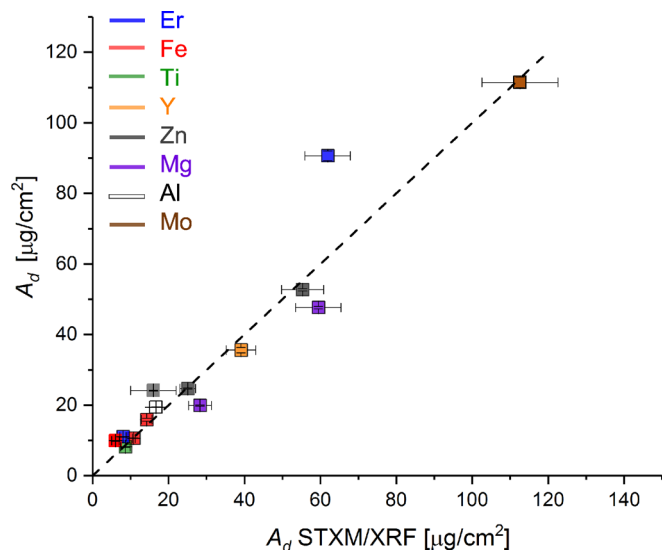

FIG. 3. (Color online) Summary of the data listed in Table III. The dashed line represents a perfect correspondence between the STXM/XRF areal density measurement and the RBS, XRR, and QCM averaged one.

into the Si_3N_4 membrane and hence provides an estimate for the maximum temperature increase of the substrate. Taking for example the trimethylaluminum (TMA) and H_2O process, we can estimate the number of surface reactive sites using the same method as that used by Routkevitch *et al.*[40] to be $\sim 0.46 \times 10^{15}$ sites/cm^2, the thickness of the TEM window is 50 nm, ΔH is 611.1 kJ/mol, and the density and specific heat of Si_3N_4 are 3.44 g/cm^3 and 800 J/(kg K), respectively. Using Eq. (5) yields a ΔT of $\sim 80\,^\circ$C. While the TMA and water ALD process has a large self-limiting temperature range (up to 345 $^\circ$C) and can handle an increase in substrate temperature during growth, many other processes, such as ZnO grown with diethylzinc (DEZ) and water, could be affected by such an increase. The ZnO process has an upper limit of 177 $^\circ$C, while the temperature increase of the Si_3N_4 membrane for a complete cycle, using Eq. (5), is $\Delta T \sim 60\,^\circ$C.

We overcame this parasitic CVD effect, noticed in early coating attempts, by either keeping the deposition temperature moderately low such that $T_{dep} + \Delta T < T_{Max}$, where T_{Max} is the upper limit of the ALD temperature range, or allowing sufficient cooling time by increasing the purge times after both half cycles. After these adjustments had been made, the coatings were highly homogenous, as illustrated in Fig. 4.

The maximal Areal density variation of the Er map (c) ($\sim 30\%$) in Fig. 4 as compared to the one in map (d) ($\sim 10\%$) could be due to the much smaller amount of Er in the Er-MgO multilayer film used for the measurement of map (c) as compared to the pure Er_2O_3 film used for map (d). For small amounts, the overlap of the Mg fluorescence spectrum K line with the Er M line renders the deconvolution procedure less reliable. The remaining 10% maximal variation in the other maps of Fig. 4 corresponds to the measurement resolution.
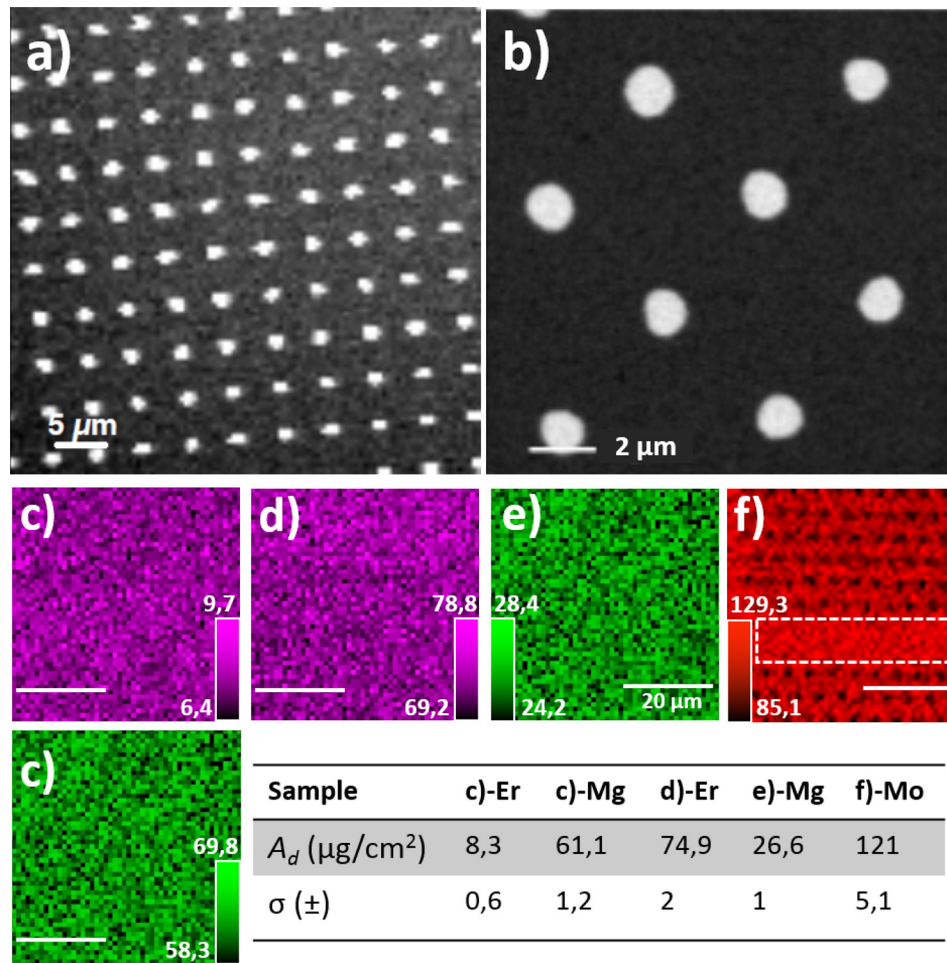
FIG. 4. (Color online) STXM and μ-XRF measurement of the ALD films deposited on perforated and plain Si₃N₄ TEM windows. (a) and (b) STXM x-ray absorption image of Fe₂O₃ coated windows acquired at (a) 718 eV ALS beamline 11.0.2 and (b) 740 eV at ALS beamline 5.3.2, showing the homogeneity of the Fe distribution over a wide area and nanometer scale. (c)–(f) μ-XRF cartographies of the Er-L edge [(c) top and (d)], Mg-K edge [(c) bottom and (e)], and Mo-L edge (f) measured at ESRF beamline 21 at 2.7 keV over 50×50 μm² with 1 μm steps. The scale bars are 20 μm. The corresponding averaged values of the areal density A_d and deviation σ are displayed in the table. For Mo, the averaged density value was taken from the plain area delimited by the dashed box in (f).

Sample	c)-Er	c)-Mg	d)-Er	e)-Mg	f)-Mo
A_d (μg/cm²)	8,3	61,1	74,9	26,6	121
σ (±)	0,6	1,2	2	1	5,1

As can be seen in Fig. 4, the use of perforated TEM windows is also viable. Depositing a conformal film on perforated windows allows for the measurement of the incident intensity, I_0, without the need to remove the standard and hence introduce possible beam fluctuations as a source of error. Sufficiently low temperature processes exist such that the deposition of ALD films on polymers has been achieved.[41,42] This points to the possibility of not only producing these standards on Si₃N₄ TEM windows but also on other materials that may be relevant in sample collection and preparation in the fields of biology and environmental science. This would allow for the direct measurement of absorption related to the substrate and alleviate the need to calculate these contributions in the measured specimens.

B. 3D standards

The SEM images [Figs. 5(a) and 5(b)] of the ALD coated cubes shown in Figs. 2(c) and 2(d) reveal a homogeneous multilayer deposition; the new dimensions of the coated cube size and edges are 6.2 μm and 1.1×2.15 μm, respectively. Compared to bare cubes, each dimension has been increased uniformly by 0.6 μm, which should coincide with

twice the total deposited film thickness. This analysis is consistent with the total film thickness of 0.311 μm measured by XRR (Table II) on witness Si coupons.

The TXM measurements and reconstruction of the coated cube [Fig. 5(b)] are shown in Figs. 5(c) and 5(f). The reconstructed cube side size is 6.4 μm, and the edge dimensions are 1.2 ± 0.1 μm $\times 2.2 \pm 0.1$ μm in very good agreement with the SEM images. The ALD multilayer coating appears as white and gray shells in Figs. 5(c)–5(e) with a total thickness of 0.35 ± 0.05 μm in concordance with the SEM and XRR measurements. The outermost white layer corresponds to the thickest and highest Z ALD layer: ZnO with an estimated thickness of 0.1 μm on the edge of this TXM measures resolution, but nonetheless consistent with XRR measurements.

These encouraging results seed future work that will involve improving the TXM resolution in order to spatially resolve the other ZnO layers of 4, 10, 20, and 40 nm deposited on the cube and test or develop reconstruction algorithms. In addition, the ZnO layers are polycrystalline as deposited on amorphous substrates with an average grain size, d, measured by XRD that depends on the film thickness. According to Ref. 43, for a 50 nm thick film, $d = 6$ nm and
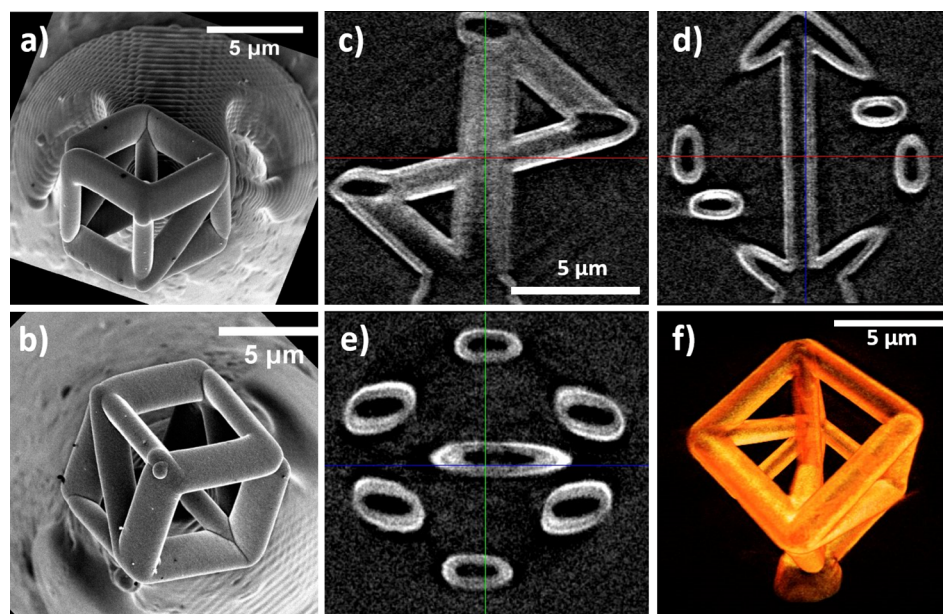
Fɪɢ. 5. (Color online) (a) and (b) SEM images of the same cubes shown in Figs. 2(c) and 2(d) after ALD coating with the Al₂O₃ and ZnO multilayer structure. The images have been rotated to match the cube orientations of Figs. 2(c) and 2(d). (c)–(f) 3D reconstruction of the ALD coated cube shown in (b) and measured at APS beamline 32-ID-C at 8 keV. (c) and (d) are cuts of the reconstructed cube (f) along specific directions. The visible white lines correspond to the outermost ALD ZnO layer with an estimated thickness of 100 nm.

for 125 nm, $d = 16$ nm with what appears to be a saturation at $d \sim 20$ nm for thicker films. This crystalline nature of ZnO in contrast to the as-grown amorphous Al₂O₃ could also be used to test the resolution limit of 3D reconstruction of nano-x-ray diffraction techniques such as diffraction tomography.

It is noteworthy to mention that the polymer nature of the cube template can restrict the ALD temperature range and hence limit the choice of compounds that can be grown. For this reason, we purposefully chose alloys that can be synthesized at low temperature (165 °C). Previous work[44,45] however has shown that pyrolysis of 3D printed structures under vacuum or an inert atmosphere at temperature between 1000 and 3000 °C can preserve the overall 3 D printed shape while reducing significantly (up to 80%) the dimensions and transforming the polymer into glassy carbons, providing stable templates for any desired ALD alloys and growth temperature.

IV. CONCLUSION

The production of reliable SR-XRF/STXM standards, either multilayer or single compound films, produced via atomic layer deposition has been demonstrated. Utilizing known chemistries, we are able to produce standards for the majority of elements throughout the periodic table, thus eliminating the need to use NIST SRM 1832/1833 standards. The conformity and uniformity of ALD produced thin films have been demonstrated using a combination of X-ray characterization, SR-XRF, STXM, XRR, RBS, and QCM. We have produced a new custom-made TEM grid sample holder that enables the simultaneous coating and fabrication of up to fifty 2D-standards, in a timely and inexpensive manner. Moreover, we have shown that the combination of ALD and

3D printing techniques provides suitable 3D standards with a controlled shape and composition that can be extended to a large variety of structures. Along those lines and as the 3D printing resolution improves with time, such synergy can be extended to the manufacturing of x-ray optics such as Fresnel zone plates, kinoform lenses, and capillaries.

[1]K. Benzerara, N. Menguy, N. R. Banerjee, T. Tyliszczak, G. E. Brown, Jr., and F. Guyot, Earth Planet. Sci. Lett. **260**, 187 (2007).
[2]M. Obst, J. J. Dynes, J. R. Lawrence, G. D. W. Swerhone, K. Benzerara, C. Karunakaran, K. Kaznatcheev, T. Tyliszczak, and A. P. Hitchcock, Geochim. Cosmochim. Acta **73**, 4180 (2009).
[3]K. Pecher, D. McCubbery, E. Kneedler, J. Rothe, J. Bargar, G. Meigs, L. Cox, K. Nealson, and B. Tonner, Geochim. Cosmochim. Acta **67**, 1089 (2003).

[4]C. Hub, M. Burkhardt, M. Halik, G. Tzvetkov, and R. Fink, J. Mater. Chem. **20**, 4884 (2010).

[5]L. Yang, R. McRae, M. M. Henary, R. Patel, B. Lai, S. Vogt, and C. J. Fahrni, Proc. Natl. Acad. Sci. U. S. A. **102**, 11179 (2005).

[6]J. Dik, K. Janssens, G. Van Der Snickt, L. van der Loeff, K. Rickers, and M. Cotte, Anal. Chem. **80**, 6436 (2008).

[7]J. Vila-Comamala *et al.*, AIP Conf. Proc. **1221**, 80 (2010).

[8]B. S. Twining, S. B. Baines, N. S. Fisher, J. Maser, S. Vogt, C. Jacobsen, A. Tovar-Sanchez, and S. A. Sańudo-Wilhelmy, Anal. Chem. **75**, 3806 (2003).

[9]T. Punshon, M. L. Guerinot, and A. Lanzirotti, Anal. Bot. **103**, 665 (2009).

[10]L. K. Moore *et al.*, New Phytol. **201**, 104 (2013).

[11]A. L. Butterworth *et al.*, Meteorit. Planet. Sci. **49**, 1562 (2014).

[12]A. S. Simionovici *et al.*, Meteorit. Planet. Sci. **49**, 1612 (2014).

[13]A. J. Westphal1 *et al.*, Science **345**, 786 (2014).

[14]M. Ritala and M. Leskelä, *Handbook of Thin Films*, edited by H. S. Nalwa (Academic, San Diego, CA, 2001), Vol. 1, pp. 103–159.

[15]M. Ritala and J. Niinisto, "Organometallic precursors for atomic layer deposition," in *Precursor Chemistry of Advanced Materials.* Topics in Organometallic Chemistry Vol 9, edited by R. A. Fischer (Springer, Berlin/Heidelberg, 2009).

[16]R. L. Puurunen, J. Appl. Phys. **97**, 121301 (2005).

[17]V. Miikkulainen, M. Leskelä, M. Ritala, and R. L. Puurunen, J. Appl. Phys. **113**, 021301 (2013).

[18]T. Proslier, J. A. Klug, J. W. Elam, H. Claus, N. G. Becker, and M. J. Pellin, J. Appl. Chem. C **115**, 9477 (2011).

[19]J. A. Klug, T. Proslier, J. W. Elam, R. E. Cook, J. M. Hiller, H. Claus, N. G. Becker, and M. J. Pellin, J. Phys. Chem. C **115**, 25063 (2011).

[20]S. C. Riha, B. M. Klahr, E. C. Tyo, S. Seifert, S. Vajda, M. J. Pellin, T. W. Hamann, and A. B. F. Martinson, ACS Nano **7**, 2396 (2013).

[21]T. W. Hamann, A. B. F. Martinson, J. W. Elam, M. J. Pellin, and J. T. Hupp, J. Phys. Chem. C **112**, 10303 (2008).

[22]S. M. George, Chem. Rev. **110**, 111 (2010).

[23]J. W. Elam and S. M. George, Chem. Mater. **15**, 1020 (2003).

[24]J. Lu, B. Fu, M. C. Kung, G. Xiao, J. W. Elam, H. H. Kung, and P. C. Stair, Science **335**, 1205 (2012).

[25]J. Niinistö, M. Putkonen, and L. Niinistö, Chem. Mater. **16**, 2953 (2004).

[26]J. A. Klug, N. G. Becker, S. C. Riha, A. B. F. Martinson, J. W. Elam, M. J. Pellin, and T. Proslier, J. Mater. Chem. A **1**, 11607 (2013).

[27]J. Aarik, J. Karlis, H. Mändar, T. Uustare, and V. Sammelselg, Appl. Surf. Sci. **181**, 339 (2001).

[28]M. Putkonen, T. Sajavaara, and L. Niinistö, J. Mater. Chem. **10**, 1857 (2000).

[29]J. Päiväsaari, J. Niinistö, K. Arstila, K. Kukli, M. Putkonen, and L. Niinistö, Chem. Vap. Deposition **11**, 415 (2005).

[30]J. A. Klug, N. G. Becker, N. R. Groll, C. Cao, M. S. Weimer, M. J. Pellin, J. F. Zasadzinski, and T. Proslier, Appl. Phys. Lett. **103**, 211602 (2013).

[31]B. L. Henke, E. M. Gullikson, and J. C. Davis, At. Data Nucl. Data Tables **54**, 181 (1993).

[32]V. A. Solé, E. Papillon, M. Cotte, P. Walter, and J. Susini, Spectrochem. Acta B **62**, 63 (2007).

[33]V. De Andrade, A. Deriy, M. J. Wojcik, D. Gürsoy, D. I. Shu, K. Fezzaa, and F. De Carlo, "SPIE Newsroom," 2016, http://spie.org/newsroom/6461-nanoscale-3d-imaging-at-the-advanced-photon-source?SSO=1.

[34]D. Gürsoy, F. De Carlo, X. Xiao, and C. Jacobsen, J. Synchrotron Rad. **21**, 1188 (2014).

[35]F. De Carlo *et al.*, J. Synchrotron Radiat. **21**, 1224 (2014).

[36]E. X. Miqueles, J. Rinkel, F. O'Dowd, and J. S. V. Bermudez, J. Synchrotron Radiat. **21**, 1333 (2014).

[37]D. Pelt, D. Gürsoy, W. J. Palenstijn, J. Sijbers, F. De Carlo, and K. J. Batenburg, J. Synchrotron Radiat. **23**, 842 (2016).

[38]D. M. Pelt and V. De Andrade, Adv. Struct. Chem. Imaging **2**, 17 (2016).

[39]G. Liu, E. Deguns, L. Lecordier, G. Sundaram, and J. Becker, ECS Trans. **41**, 219 (2011).

[40]D. Routkevitch, P. P. Mardilovich, and S. M. George, Chem. Mater. **15**, 3507 (2003).

[41]J. W. Elam, C. A. Wilson, M. Schuisky, Z. A. Sechrist, and S. M. George, J. Vac. Sci. Technol., B **21**, 1099 (2003).

[42]T. K. Minton, B. Wu, J. Zhang, N. F. Lindholm, A. I. Abdulagatov, J. O'Patchen, S. M. George, and M. D. Groner, ASC Appl. Mater. Interfaces **2**, 2515 (2010).

[43]A. A. Chaaya *et al.*, Beilstein J. Nanotechnol. **4**, 690 (2013).

[44]J. Bauer, A. Schroer, R. Schwaiger, and O. Kraft, Nat. Mater. **15**, 438 (2016).

[45]See supplementary material at https://doi.org/10.1116/1.5025240 for the X-Ray Reflecitivity data measured for the films listed in Tables II and III along with the corresponding fits. Each film thickness and density extracted from the fits are described in the figure captions.